Highly Sensitive Fiber Taper Interferometric Hydrogen Sensors
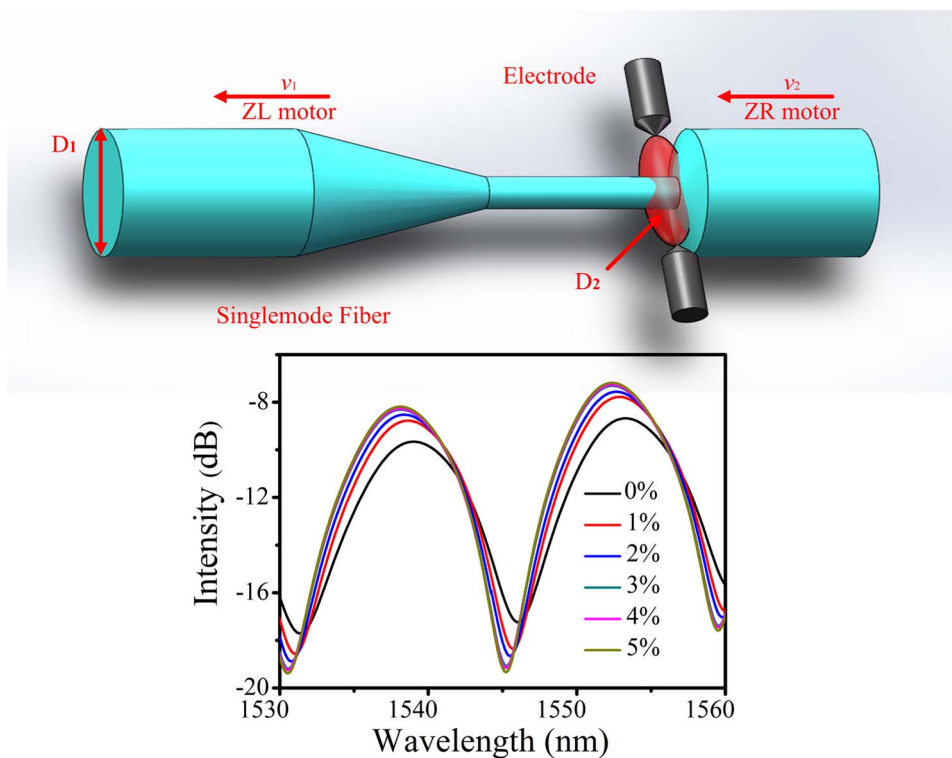
Zhipeng Yu
Long Jin
Lipeng Sun
Jie Li
Yang Ran
Bai-Ou Guan

Highly Sensitive Fiber Taper Interferometric Hydrogen Sensors

Zhipeng Yu, Long Jin, Lipeng Sun, Jie Li, Yang Ran, and Bai-Ou Guan

Guangdong Provincial Key Laboratory of Optical Fiber Sensing and Communications, Institute of Photonics Technology, Jinan University, Guangzhou 510632, China

Abstract: We report on the implementation of fiber taper interferometric hydrogen sensors with high sensitivity and good reproducibility. The tapering process is carried out with a commercial fusion splicer by precisely controlling the pulling and feeding velocities, as well as arc strength. The taper can naturally act as a Mach–Zehnder interferometer and intrinsically offers a transmission spectrum with periodic interference fringes. The sensor with a waist diameter of 3.0 μm can present a spectral shift up to -1.99 nm when injecting hydrogen with a concentration of 5% as a result of strong evanescent field interaction with the Palladium overlay. We have fabricated a number of sensors with identical parameters and found that the relative error ratio in waist diameter is less than 6% and that in hydrogen response is 4.2%.

Index Terms: Fiber taper interferometer, hydrogen sensors, optical microfibers.

1. Introduction

Fiber optic hydrogen sensors have recently been proposed and developed for applications in clean energy and aerospace industries [1]. The implementation of a fiber hydrogen sensor typically relies on Palladium coating on fiber surface. The Pd overlay expands in volume and stretches the fiber when absorbing molecular hydrogen, resulting in variations of optical signals in terms of intensity, phase and/or wavelength. A number of sensor schemes have been demonstrated, including interferometers, fiber gratings, and endface absorbers [2]–[5]. However, the conventional expand-stretch approach cannot offer satisfactory response to hydrogen, especially compared to the intrinsic temperature response of optical fibers. Take a Pd-coated FBG for instance, the Bragg wavelength can shift by only tens of picometers with the existence of hydrogen. The temperature sensitivity, in contrast, reaches 10 pm/$^\circ$C, which can possibly cause failure of hydrogen detection. The weak response to hydrogen is a result of the significant difference in volume between the silica fiber and the Pd overlay. Alternatively, evanescent sensors can be implemented, exploiting the evanescent field interaction between light and the Pd overlay, in order to enhance the sensitivity. Possible strategies include side-polishing, femtosecond laser micromachining, or simply tapering the fiber down to microscale diameters [6]–[8]. Tapered
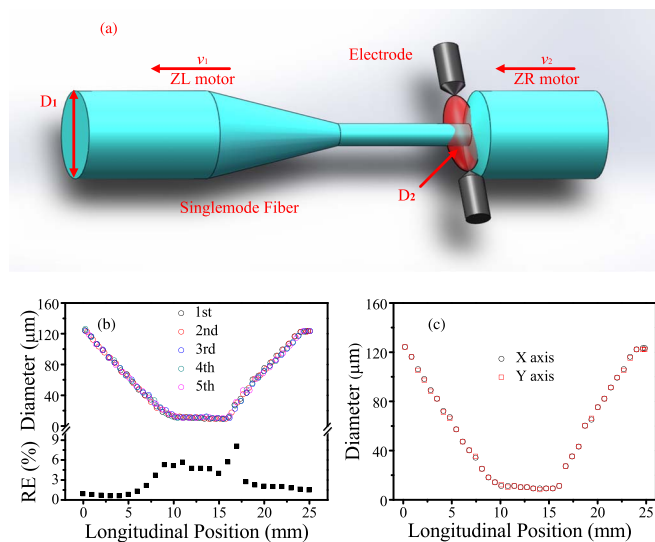
Fig. 1. (a) Schematic of fiber tapering via arc discharge. v_1: Pulling speed, v_2: Feeding speed, $D_{1]}$: Diameter of the singlemode fiber, D_2: Waist diameter. (b) (Top) Measured longitudinal profiles of local diameter for five individual tapers. (Bottom) Relative error (RE) in taper diameter. The taper length is 2.5 cm. (c) Measured taper geometry along two orthogonal directions.

optical micro- and nano-fibers have strong evanescent fields and can "see" the small changes in surrounding environments. The ability of a subwavelength optical fiber as a gas sensor has been exhibited based on evanescent absorptions. Subsequently, silica microfiber devices including Bragg gratings [9], Mach–Zehnder interferometer [10], knot resonators [11], and microstructured fiber tapers [12], [13] have been exploited as sensors to detect molecular hydrogen and other gases.

On the other hand, the geometrical control and tailoring of fiber tapers or microfibers have been intensively studied [14]–[24]. Fiber tapers with complex transverse and longitudinal profiles have been demonstrated towards applications including optical nonlinearity, mode couplers, and photonic sensors. However, there is still a long way for microfiber or fiber taper sensors approaching practical applications, since the tapers fabricated by conventional flame-brush method is hardly reproducible in geometry and typically has a length over 10 cm. For sensing applications, fiber tapers with relatively short length (less than 3 cm), convenient fabrication, and high structural reproducibility are required. In addition, it is favorable if a fiber taper intrinsically offers an optical signal in terms of change in intensity, wavelength, or phase in response to measurands. To fulfill these requirements, in this work, we present reproducible fabrication of fiber taper interferometric sensors via precisely controlled arc discharge and demonstrate their exploration as a highly sensitive hydrogen sensor. Based on the strong evanescent field interaction, a taper interferometer with a waist diameter of 3 μm and a 4-nm thick Pd overlay presents a spectral shift of –1.99 nm to 5% hydrogen exposure and a temperature sensitivity as low as $-15\,\mathrm{pm/^\circ C}$. Experimental result suggests that the relatively error of waist diameter is less than 6%. The reproducibility of the microfibers presents a low relative error ratio of 4.2% in response to hydrogen. The present fabrication of fiber taper sensors with high sensitivity and good reproducibility in both geometry and sensor performance makes a solid step towards practical applications.

2. Fabrication Of Fiber Tapers

Fig. 1(a) shows the schematic of the fiber tapering process, carried out by use of a commercial fusion splicer (Fujikura, FSM100P+). The continuous arc discharge generated by the fixed electrodes act as a source to heat the fiber over a localized region. During the arc discharge, the

TABLE 1

Specific parameters of tapering process of three steps. $r = D_2/D_1$ and $v_{feed} = 0.01 \, \mu m/ms$

Procedure	Step 1		Step 2		Step 3	
Arc duration	$\dfrac{(r^2 + r + 1) \cdot L_1}{3 v_{feed}}$		$\dfrac{L_2}{v_{max}}$		$\dfrac{(r^2 + r + 1) \cdot L_3}{3 v_{feed}}$	
Motor	ZL	ZR	ZL	ZR	ZL	ZR
Initial velocity ($\mu m/ms$)	0.01	0.01	1	0.01	$(\dfrac{6}{1+r+r^2}-1) \cdot v_{feed}$	0.01
Acceleration ($\mu m/ms^2$)	$\dfrac{2-r-r^2}{(1+r+r^2)^2} \cdot \dfrac{6 v_{feed}^2}{L_1}$	0	0	0	$\dfrac{r^2-r-2}{(1+r+r^2)^2} \cdot \dfrac{6 v_{feed}^2}{L_3}$	0

right fiber holder carried by ZR motor moves towards the electrodes with a constant velocity $v_{feed} = 0.01 \, \mu m/ms$ to feed the silica material into the hot zone. The left fiber holder carried by the ZL motor moves against the electrodes with velocity v_{pull} to draw the softened glass out of the hot zone. The desired geometry is formed by controlling the pulling and feeding speeds in combination of arc strength.

The taper process can be divided into three consecutive steps, corresponding to the formation of left transition region, uniform waist region and right transition region with lengths of L_1, L_2, and L_3 (here $L_1 = L_3$ for simplicity), respectively. Table 1 lists the optimal parameters for all the three steps. In [14] the authors have described the basic law of fiber tapering—the conservation of mass and depicted how to determine the taper geometry with a scanning or a length-varying heat source. The mass conservation also applies to our method, in terms of equality between the mass feeding rate into the hot zone and the pulling rate out of there. In step 1 during the formation of the first transition region whose local diameter almost linearly changes from D_1 to D_2, the left motor moves with an initial velocity that equals to v_{feed} and an acceleration of $\alpha = (2 - r - r^2)/(1 + r + r^2)^2 \cdot 6 v_{feed}^2/L_1$, derived from the mass conservation condition. In step 2, the velocity of ZL motor abruptly changes to $v_{max} = 1 \mu m/ms$ and then keeps constant to form a uniform waist. This motor runs so fast compared to ZR motor that the local diameter can maintain at D_2. Step 3 begins with an initial pulling speed $v = (5 - r - r^2)/(1 + r + r^2) \cdot v_{feed}$ and a deceleration α to form a symmetric taper structure. The arc strength is also optimized for different local taper diameters to form smooth fiber tapers. It has a correlation in the individual steps. For example, for target waist diameter of 5.8 μm, the initial pulling speed v_{pull} is 0.01 μm/ms and increases to 0.047 μm/ms with an acceleration of $1.06 \times 10^{-6} \mu m/ms^2$ in step 1 and forms a transition region from 125 to 5.8 μm in diameter. The arc strength gradually changes from 13.1 to 12.8 mA. In step 2, the motion of ZL motor begins with an abrupt change to a velocity of 1 μm/ms and remains unchanged over the whole waist region. The arc strength keeps at 12.8 mA. The velocity of the ZL motor changes suddenly to 0.047 μm/ms in the beginning of step 3 and decreases gradually to 0.01 μm/ms with a deceleration of $1.06 \times 10^{-6} \mu m/ms^2$. The corresponding arc strength increases from 12.8 mA to 13.1 mA to form the other transition region. Fig. 1(b) shows the measured longitudinal profiles of five individual fiber tapers fabricated with identical parameters. The designed taper length is 2.5 cm. The waist region has a length of 6 mm and a diameter of 9 μm. The relative errors in taper diameter are below 6% over the uniform region and below 3% over the transition regions. The size error reaches almost 8% at around the second turning point between the waist and the transition region, which is caused by the abrupt change of v_{pull}. Fig. 1(c) shows the profiles of a single taper observed from two orthogonal directions, which presents its good symmetry.

To demonstrate the flexibility of the fiber tapering process, we have fabricated tapers with different lengths of the waist and transition regions and observe their transmission spectra. Fig. 2
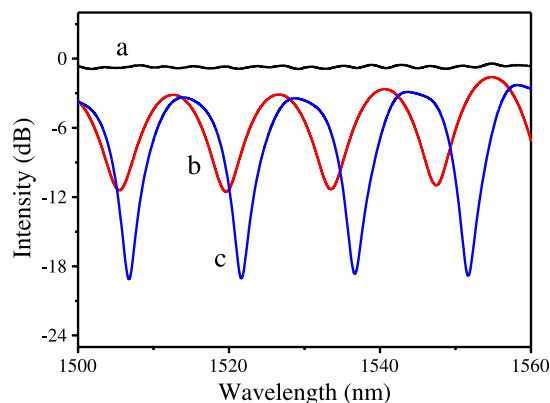
Fig. 2. Measured transmission spectra of different fiber tapers. Samples a and b are drawn from conventional singlemode fibers with taper angles of 0.35 and 4 degrees, respectively. Sample c is drawn from a double cladded singlemode fiber with a taper angle of 4 degrees.

shows the transmission spectra of three taper samples. Samples a and b are drawn from conventional 125 μm G-652 singlemode fibers to 8 μm in diameter. Their taper angles are 0.35 and 4 degrees, and the total lengths are 25 mm and 5 mm, respectively. The former can be approximately considered as an adiabatic taper with an average transmission loss of –0.8 dB. The periodic variation in the spectrum is a result of weak local mode couplings. For sample b with a larger taper angle, the fundamental HE_{11} mode can be partially coupled to higher order modes over the transition region, mainly HE_{12} mode here. As a result, the two transition regions act a mode splitter and combiner, respectively, and the taper is naturally a Mach–Zehnder interferometer. Periodic interference fringes can be observed in the transmission spectrum, due to the phase difference between the two modes. The average transmission loss is 3 dB, due to the couplings to higher order modes. The extinction ratio increases with taper angle as a result of more coupled fractional energy. The maximum taper angle limit is about 6 degree, over which the transmission loss significantly rises. The minimum length of the whole taper can be as short as 3.8 mm, which offers an alternative option for compact device and sensor applications, and the minimum waist diameter can be as small as 3 μm. Sample c in is drawn from a double cladded singlemode fiber (CorActive Corporation), and the mode field diameter and the numerical aperture of this fiber are 6.6 μm and 0.2, respectively. The taper angle is also 4 degree, and the length and diameter is 5 mm and 8 μm, respectively, identical to sample b. In contrast, this taper presents much higher extinction ratio, because this double cladded fiber contains an index-reduced F-doped inner cladding. The HE_{12} local mode tends to extend to the pure-silica outer cladding at the transition regions which results in a higher coupling ratio [25]. This taper interferometer with high extinction ratio is then exploited as a hydrogen sensor in the following text.

3. Sensor Implementation and Characterization

The taper interferometer is placed in a vacuum chamber for the deposition of Palladium by using magnetron sputtering driven by an RF source. It is rotated for a single round during sputtering within 20 seconds by use of two rotatable fiber holders and a uniform Pd overlay with a thickness of only 4 nm can be coated. The average transmission loss increases by 6 dB, which is attributed to absorption by the Pd overlay. Fig. 3 shows the schematic setup for the measurement of hydrogen response and the SEM image of the Pd coated sensor. The Pd coated fiber taper is placed in a gas chamber where hydrogen with a certain concentration is injected. The concentration is determined by controlling the flow rates of pure N_2 and H_2/N_2 mixture (5%/95%). The transmission spectrum of the sensor is recorded by use of a broadband light source (1250–1650 nm) and an optical spectrum analyzer (Yokogawa, AQ6370C) with a resolution of 0.1 nm.
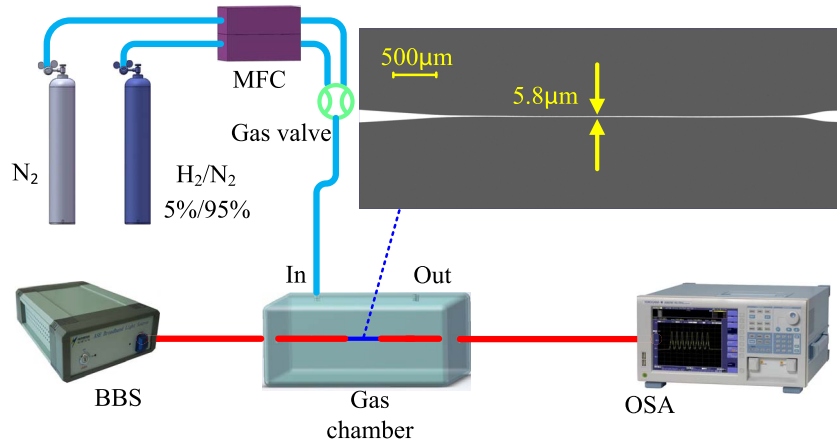
Fig. 3. Experimental setup of the fiber taper interferometric hydrogen sensor. BBS: Broadband light source; OSA: Optical spectrum analyzer; MFC: Mass flow controller. The hydrogen concentration is determined by controlling the flow rate contrast between the two channels. (Inset) SEM image of the taper sensor.
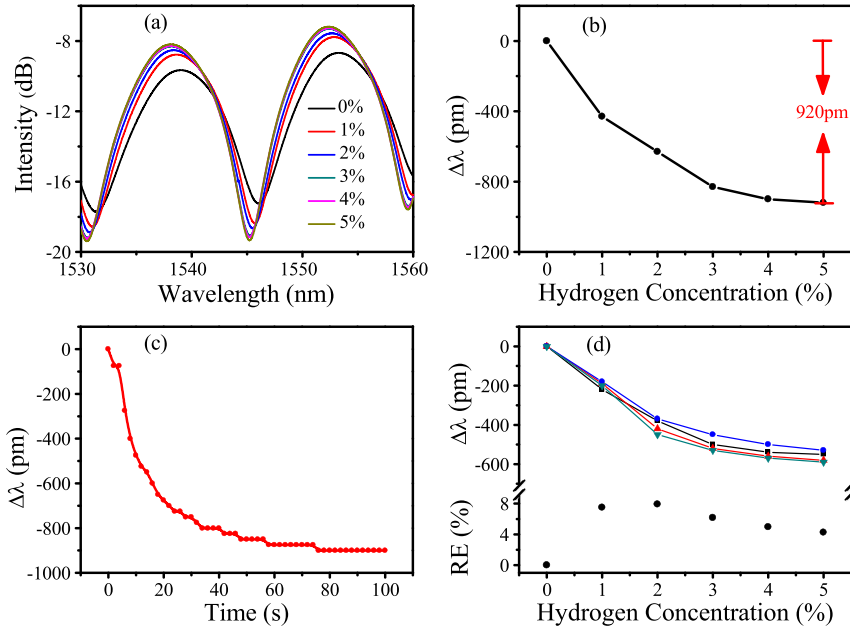

Fig. 4. (a) Measured transmission spectra of a Pd-coated fiber taper interferometer with H_2 concentrations from 0 to 5%. The taper has a waist diameter of 4.5 μm. (b) Measured wavelength shift as a function of H_2 concentration of the dip at around 1545 nm. (c) Time response in terms of wavelength shift with sudden hydrogen injection with a concentration of 5%. (d) (Top) Measured wavelength shifts as a function of H_2 concentration for four individual sensors as a reproducibility test. (Bottom) The relative error (RE) of the wavelength shifts with H_2 concentrations from 0 to 5%.

Fig. 4(a) shows the measured spectra of a Pd coated taper interferometer with different H_2 concentrations. The taper has a waist diameter of 4.5 μm. The whole transmission spectrum blue shifts with increasing H_2 concentration. Fig. 4(b) shows the measured wavelength shift as a function H_2 concentration. A selected transmission dip at around 1545 nm shifts by −920 pm with a hydrogen concentration of 5%. The dip wavelength changes faster with lower H_2 concentration, due to the phase change of the PdH_x complex and the resultant nonlinear refractive-index change. Fig. 4(c) shows the time response of the sensor. In this measurement, the
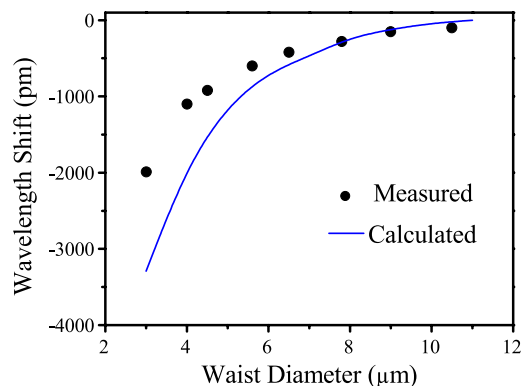
Fig. 5. Measured and calculated wavelength shifts with exposure to 5% hydrogen as a function of waist diameter.

sensor is placed into a smaller gas chamber with a capacity of 120 mL, then a concentration of 5% hydrogen with a flow rate of 500 mL/min is immediately injected. The measured response time is about 30 seconds. Note that the Pd overlay is only 4 nm in thickness, which is much thinner than that for the conventional expand-stretch sensor schemes, typically 500 nm [26], which enables fast response to the existence of hydrogen. Thicker Pd coating does induce stronger response to H_2 exposure, but can also bring higher absorption losses, especially for the higher-order modes, which can probably lead to a much lower extinction ratio and make the transmission dips difficult to distinguish.

To test the repeatability of the sensor, the spectral shift of a 5.8 μm Pd coated taper interferometer is recorded with five cycles of H_2 injection and removal. The measured shifts with 5% H_2 for the individual cycles are –500 pm, –550 pm, –480 pm and –490 pm, and –550 pm, respectively. The maximal difference in spectral response is 70 pm and the relative error ratio is 5.8%. The difference in performance for each cycle may be a result of imperfection of Pd overlay bonding with the optical fiber. To examine the reproducibility of the sensor, we further fabricated four 6 μm tapers with identical parameters, coated them with Pd film, and measured their response to H_2. Fig. 4(d) shows the measured responses. The individual spectral shifts with 5% hydrogen concentration are –530 pm, –580 pm, –590 pm, and –550 pm, respectively. The maximal difference is 60 pm, and the relative error ratio is 4.2%. The sputtering parameters have been optimized to obtain a uniform overlay as possible as we can. However, there might be some nonuniformities in overlay thickness along the taper, which can possibly contribute to the difference in optical response for the individual samples. Further efforts will be made to improve the overlay uniformity for better reproducibility. The good repeatability and reproducibility of the present sensor are important for the further exploration towards practical applications in the clean energy and aerospace industries.

We have measured the hydrogen responses of fiber tapers with different waist diameters. The thickness of the Pd film is almost unchanged for different sensors. Fig. 5 shows the measured wavelength shifts with 5% hydrogen concentration as a function of fiber diameter. The sensor with a waist diameter of 3.0 μm can present a spectral shift up to –1.99 nm when exposed to hydrogen with a concentration of 5%. Compared with the sensing schemes including the side polished Bragg grating [6], the fs-laser micromachined interferometer [7], microfiber Bragg gratings [9], and the microfiber knot resonator [11], the present sensor presents higher wavelength sensitivity. The long period grating pair sensor in [5] exhibits a comparable sensitivity, but much thicker sensitive overlay is needed. The plasmonic interferometric sensor incorporating a section of PdAu nanowire in [10] presents higher sensitivity at low hydrogen concentrations, but the assembly between the nanowire and silica microfiber is quite complex.

When absorbing molecular hydrogen, the PdH_x overlay tends to expand in volume and stretch the fiber taper. The overlay also changes in refractive index (both real and imaginary

parts) and varies the effective indexes of the optical modes via evanescent field interaction. Based on the theory in [25], the total hydrogen sensitivity can be expressed

$$\frac{d\lambda}{dc} = \frac{\lambda}{\Gamma}\left[\frac{\partial(\Delta n)/\Delta n}{\partial n_{(pd,c)}} \cdot \frac{n_{(pd,0)} \cdot d\sqrt{h(c)}}{dc} + (1 + p_e)\frac{d\varepsilon}{dc}\right] \qquad (1)$$

where λ is the dip wavelength, and c denotes the hydrogen concentration. This equation has taken into account the effect of modal dispersion by introducing a dispersion factor $\Gamma = 1 - (\lambda/\Delta n)(\partial\Delta n/\partial\lambda)$. It typically has a negative value as described in [13]. The first term in the bracket depicts the contribution of evanescent field interactions. Here Δn represents the mode index difference between the HE_{11} and HE_{12} modes, n_{pd} denotes the real part of the refractive index of the Pd overlay. When c equals 0, $n_{(pd,0)}$ can take a value of 3 at around 1550 nm [27]. The term $(\partial(\Delta n)/\Delta n)/\partial n_{(pd,c)}$ depicts the interaction strength, whose value can be calculated with a finite-element-method (FEM) based mode solver. Specifically, the spatial distribution of permittivity is first defined, with the refractive indexes (real parts) 1.444 and 1.458, and 3.0 for pure silica, germanium doped silica and Pd overlay, respectively. The thickness of the overlay is set as 4 nm. The mode indexes of the HE_{11} and HE_{12} modes are numerically calculated with an initial overlay refractive index and then the mode-solving is carried out again with a slightly varied overlay index. The RI decrease of the Pd overlay results in mode-index decreases of both HE_{11} and HE_{12} modes with different rates. As a result, the index difference increases with the absorption of H_2 and leads to the blue shift in spectrum. The factor $h(c) = (n_{(pd,c)}/n_{(pd,0)})^2$ is a nonlinear function associated with the phase change of PdH_x. It decreases with the hydrogen concentration c and taking values less than 1 [1], [28]. Therefore the amplitude of the term $n_{(pd,0)} \cdot d\sqrt{h(c)}/dc$ is intrinsically determined by the PdH_x overlay. Based on the calculation method described above, the contribution of the evanescent field interaction for a 4.5 μm sensor is about -1500 pm at 5% hydrogen concentration. The second term in the bracket gives the contribution of deformation induced by the Pd overlay expansion. The factor $p_e = \partial(\Delta n)/(\Delta n \cdot \partial\varepsilon)$ is the effective elastic optic coefficient, which is associated with the variation of HE_{11}/HE_{12} mode-index difference induced by Pd film expansion. The axial strain ε induced by hydrogen absorption is defined as follows [4]:

$$\varepsilon = \frac{0.026\sqrt{\sigma c}}{K}\left[\frac{(b^2 - a^2)Y_{pd}}{a^2 Y_{si+((b^2-a^2)Y_{pd})}}\right] \qquad (2)$$

where $\sigma = 760$ Torr is a standard atmospheric pressure, $K = 350\,\text{Torr}^{1/2}$ is the Sievert's coefficient, and a and b are the diameters of the waist diameter and outside diameter of the coated sensor, respectively. $Y_{pd} = 121$ GPa and $Y_{si} = 73$ GPa are the Young moduli of the Pd coating and silica glass, respectively. Based on (2), the expansion induced response is only -4 pm in spectral shift. Compared to the evanescent counterpart, we can determine that spectral shift is dominated by the evanescent-field interaction. We have calculated the response to H_2 with different waist diameters and the result is superimposed in Fig. 5, which suggests that thinner fiber tapers enables stronger response, due to the stronger evanescent field interactions. The deviation between the calculated and measured result may arise from the uncertainties about the index change of the extremely thin Pd overlay.

Fig. 6 shows the measured temperature responses for a taper interferometer before and after Pd coating. The uncoated taper presents a temperature sensitivity of only -5 pm/$^\circ$C, because of the thermo-optic effect and the thermal expansion of the silica fiber. The coated microfiber presents a sensitivity of up to -15 pm/$^\circ$C, raised by three times. The temperature sensitivity of the uncoated taper interferometer can be expressed by

$$\frac{d\lambda}{dT} = \lambda\frac{1}{\Gamma}\left(\alpha_{si} + \frac{\beta_{si}}{\Delta n}\frac{\partial\Delta n}{\partial n_{si}}\right) \qquad (3)$$
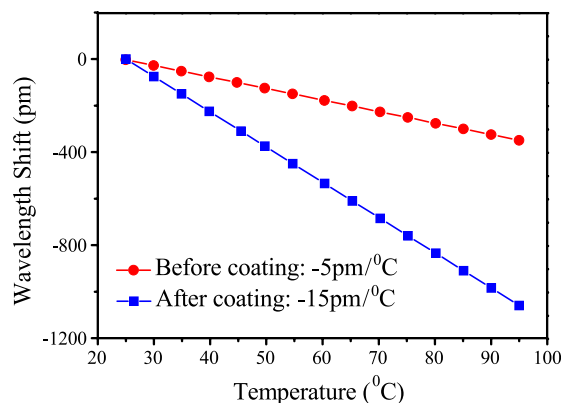
Fig. 6. Measured wavelength shifts with temperature for fiber taper interferometer before and after Pd coating. The waist diameter is 5 μm.

where $\alpha_{si} = 5 \times 10^{-7}/°C$ is the thermal-expansion coefficient, and $\beta_{si} = dn_{si}/dT = 6 \times 10^{-6}/°C$ is the thermo-optic coefficient of silica glass. The calculated result for the bare taper temperature sensitivity is $-5.5\,\text{pm}/°C$, in agreement with the measured result. Based on the theory in [4], the contribution of thermal expansion of Pd overlay to the change in thermal response of the sensor can be expressed as

$$\frac{d\lambda_{pd}}{dT} = \frac{\lambda}{\Gamma} \left[\frac{(b^2 - a^2)Y_{pd}}{a^2 Y_{si} + ((b^2 - a^2)Y_{pd})} \right] \alpha_{pd} \qquad (4)$$

where $\alpha_{pd} = 11.8 \times 10^{-6}/°C$ is thermal expansion coefficient of Pd coating. Substituting the geometrical and material parameters into (4), the contribution of Pd expansion to the temperature sensitivity is estimated as only $-0.04\,\text{pm}/°C$. Therefore, the change in temperature sensitivity is attributed to the change in optical and mechanical characteristics of the Pd overlay. However, the temperature dependencies of these characteristics are not fully clear to us so far and the quantitative analysis cannot be finished here.

4. Conclusion

We have presented fiber taper interferometric hydrogen sensors with both high sensitivity and good reproducibility. The sensors are fabricated by tapering a double cladded singlemode fiber via arc discharge by use of a commercial fusion splicer. The wavelength shift reaches −1.99 nm when exposed to hydrogen with a concentration of 5%, as a result of the strong evanescent field interaction with the Palladium overlay. By precisely controlling the motions and the arc strength, the relative error in waist diameter is less than 6%. As to the sensor performance, the relative error ratio is only 4.2% for the individual sensors. The good reproducibility and high sensitivity is greatly beneficial for the applications in clean energy and aerospace industries.

References

[1] X. Bévenot, A. Trouillet, C. Veillas, H. Gagnaire, and M. Clément, "Hydrogen leak detection using an optical fibre sensor for aerospace applications," *Sens. Actuators B, Chem.*, vol. 67, no. 1/2, pp. 57–67, Aug. 2002.
[2] M. A. Butler, "Micromirror optical fiber hydrogen sensor," *Sens. Actuators B, Chem.*, vol. 22, no. 4, pp. 155–163, Nov. 1994.
[3] F. Zhou, S. J. Qiu, W. Luo, F. Xu, and Y. Q. Lu, "An all-fiber reflective hydrogen sensor based on a photonic crystal fiber in-line interferometer," *IEEE Sensors J.*, vol. 14, no. 4, pp. 1133–1136, Apr. 2014.
[4] B. Sutapun, M. Tabib-Azar, and A. Kazemi, "Pd-coated elastooptic fiber optic Bragg grating sensors for multiplexed hydrogen sensing," *Sens. Actuators B, Chem.*, vol. 60, no. 1, pp. 27–34, Nov. 1999.
[5] Y. H. Kim, M. J. Kim, M. Park, J. Jang, and B. H. Lee, "Hydrogen sensor based on a palladium-coated long-period fiber grating pair," *J. Opt. Soc. Korea*, vol. 12, no. 4, pp. 221–225, Dec. 2008.

[6] J. Dai *et al.,* "Side-polished fiber Bragg grating hydrogen sensor with WO_3-Pd composite film as sensing materials," *Opt. Exp.*, vol. 19, no. 7, pp. 6141–6148, Mar. 2011.

[7] M. Wang *et al.,* "Femtosecond laser fabricated micro Mach–Zehnder interferometer with Pd film as sensing materials for hydrogen sensing," *Opt. Lett.*, vol. 37, no. 11, pp. 1940–1942, Jun. 2012.

[8] J. Villatoro and D. Monzón-Hernández, "Fast detection of hydrogen with nanofiber tapers coated with ultrathin palladium layers," *Opt. Exp.*, vol. 13, no. 13, pp. 5087–5092, Jun. 2005.

[9] Z. Yu *et al.,* "Microfiber Bragg grating hydrogen sensors," *IEEE Photon. Technol. Lett.*, vol. 27, no. 24, pp. 2575–2578, Dec. 2015.

[10] F. Gu, G. Wu, and H. Zeng, "Hybrid photon–plasmon Mach–Zehnder interferometers for highly sensitive hydrogen sensing," *Nanoscale*, vol. 7, no. 3, pp. 924–929, Jan. 2015.

[11] X. Wu, F. Gu, and H. Zeng, "Palladium-coated silica microfiber knots for enhanced hydrogen sensing," *IEEE Photon. Technol. Lett.*, vol. 27, no. 11, pp. 1228–1231, Jun. 2015.

[12] D. Monzón-Hernández, V. P. Minkovich, J. Villatoro, M. P. Kreuzer, and G. Badenes, "Photonic crystal fiber microtaper supporting two selective higher-order modes with high sensitivity to gas molecules," *Appl. Phys. Lett.*, vol. 93, no. 8, Aug. 2008, Art. ID 081106.

[13] V. P. Minkovich and D. Monzón-Hernández, "Microstructured optical fiber coated with thin films for gas and chemical sensing," *Opt. Exp.*, vol. 14, no. 18, pp. 8413–8418, Sep. 2010.

[14] T. A. Birks and Y. W. Li, "The shape of fiber tapers," *J. Lightw. Technol.*, vol. 10, no. 4, pp. 432–438, Apr. 1992.

[15] G. Brambilla, V. Finazzi, and D. J. Richardson, "Ultra-low-loss optical fiber nanotapers," *Opt. Exp.*, vol. 12, no. 10, pp. 2258–2263, May 2004.

[16] Y. K. Lize *et al.,* "Microstructured optical fiber photonic wires with subwavelength core diameter," *Opt. Exp.*, vol. 12, no. 14, pp. 3209–3217, Jul. 2004.

[17] F. Bayle and J. P. Meunier, "Efficient fabrication of fused-fiber biconical taper structures by a scanned CO_2 laser beam technique," *Appl. Opt.*, vol. 44, no. 30, pp. 6402–6411, Oct. 2005.

[18] S. Pricking and H. Giessen, "Tapering fibers with complex shape," *Opt. Exp.*, vol. 18, no. 4, pp. 3426–3437, Feb. 2010.

[19] L. Ding, C. Belacel, S. Ducci, G. Leo, and I. Favero, "Ultralow loss singlemode silica tapers manufactured by a microheater," *Appl. Opt.*, vol. 49, no. 13, pp. 2441–2445, May 2010.

[20] C. Baker and M. Rochette, "A generalized heat-brush approach for precise control of the waist profile in fiber tapers," *Opt. Mater. Exp.*, vol. 1, no. 6, pp. 1065–1076, Oct. 2011.

[21] A. Felipe, G. Espindola, H. J. Kalinowski, J. A. S. Lima, and A. S. Paterno, "Stepwise fabrication of arbitrary fiber optic tapers," *Opt. Exp.*, vol. 20, no. 19, pp. 893–904, Aug. 2012.

[22] H. L. Sørensen, E. S. Polzik, and J. Appel, "Heater self-calibration technique for shape prediction of fiber tapers," *J. Lightw. Technol.*, vol. 32, no. 10, pp. 1886–1891, May 2014.

[23] I. Hernández-Romano *et al.,* "Highly sensitive temperature sensor based on a polymer-coated microfiber interferometer," *IEEE Photon. Technol. Lett.*, vol. 27, no. 24, pp. 2591–2594, Dec. 2015.

[24] G. Salceda-Delgado, D. Monzon-Hernandez, A. Martinez-Rios, G. A. Cardenas-Sevilla, and J. Villatoro, "Optical microfiber mode interferometer for temperature-independent refractometric sensing," *Opt. Lett.*, vol. 37, no. 11, pp. 1974–1976, Jun. 2012.

[25] Y. Tan, L. P. Sun, L. Jin, J. Li, and B. O. Guan, "Temperature-insensitive humidity sensor based on a silica fiber taper interferometer," *IEEE Photon. Technol. Lett.*, vol. 25, no. 22, pp. 2201–2204, Nov. 2013.

[26] M. Buric, T. Chen, M. Maklad, P. R. Swinehart, and K. P. Chen, "Multiplexable low temperature fiber Bragg grating hydrogen sensors," *IEEE Photon. Technol. Lett.*, vol. 21, no. 21, pp. 1594–1596, Nov. 2009.

[27] M. A. Ordal *et al.,* "Optical properties of the metals, Al, Co, Cu, Au, Fe, Pb, Ni, Pd, Pt, Ag, Ti and W in the infrared and far infrared," *Appl. Opt.*, vol. 22, no. 7, pp. 1099–1119, Apr. 1983.

[28] X. Bévenot, A. Trouillet, C. Veillas, H. Gagnaire, and M. Clément, "Surface plasmon resonance hydrogen sensor using an optical fiber," *Meas. Sci. Technol.*, vol. 13, no. 1, pp. 118–124, Dec. 2002.